Phase-Resolved Surface Plasmon Interferometry of Graphene

Justin A. Gerber, Samuel Berweger,[*] Brian T. O'Callahan, and Markus B. Raschke[†]
Department of Physics, Department of Chemistry, and JILA, University of Colorado, Boulder, Colorado 80309, USA

(Received 7 February 2014; published 30 July 2014)

The surface plasmon polaritons (SPPs) of graphene reflect the microscopic spatial variations of underlying electronic structure and dynamics. Here, we excite and image the graphene SPP response in phase and amplitude by near-field interferometry. We develop an analytic cavity model that can self-consistently describe the SPP response function for edge, grain boundary, and defect SPP reflection and scattering. The derived SPP wave vector, damping, and carrier mobility agree with the results from more complex models. Spatial variations in the Fermi level and associated variations in dopant concentration reveal a nanoscale spatial inhomogeneity in the reduced conductivity at internal boundaries. The additional SPP phase information thus opens a new degree of freedom for spatial and spectral graphene SPP tuning and modulation for optoelectronics applications.

DOI: 10.1103/PhysRevLett.113.055502 PACS numbers: 81.05.ue, 07.79.Fc, 73.20.Mf

The light-matter interaction of graphene is distinct from that of other forms of matter due to its unique electronic band structure. The high quantum yield has already enabled a range of optoelectronics and photonic applications based on single particle excitations. However, even more unusual are the collective particle excitations in the form of Dirac plasmons, typically in the infrared spectral range, with their properties controllable by electric field gating, doping, or multilayer stacking [1–5]. In the long wavelength limit, the unique properties of massless Dirac fermions lead to a very large reduction of surface plasmon polariton (SPP) wavelength compared to the free-space excitation wavelength: $\lambda_{\mathrm{SPP}}/\lambda_0 \simeq 2\alpha E_F/(\epsilon\hbar\omega) \sim \alpha$ [6], with fine structure constant α and Fermi energy E_F. The short SPP wavelength gives rise to a strong spatial confinement, but the momentum mismatch due to the associated large in-plane wave vector concomitantly requires high k-vector field components for the SPP excitation. That coupling can be achieved through the near field of dipolar emitters [7,8] or nanostructures such as the pointed apex of a scanning probe tip [9–11]. In particular, using a tip to excite and subsequently scatter the polarization of the Dirac plasmons into detectable far-field radiation, the expected deep-subwavelength SPP standing wave from boundary reflections at mid-IR frequencies could be imaged using scattering-type scanning near-field optical microscopy (s-SNOM) [12–15].

The plasmon wavelength, its damping, and other spatial details directly relate to the local electronic structure, which is determined by doping or strain [1,2,16], the number of layers, and their stacking order [5,17,18], and is further modified by atomic scale discontinuities at edges, grain boundaries, and defects. With the exquisite sensitivity of the spatial plasmon response to these parameters, near-field plasmon interferometry can serve as a sensitive probe for the electronic structure and its spatial inhomogeneities, which are difficult to access by other techniques. So far, however, near-field imaging experiments have only analyzed the amplitude of the optical response [12–15].

For a complete understanding of the correlation between the optical near-field response and the underlying electronic structure, a full spatial characterization of the plasmon amplitude and phase is desirable. Such complementary information would allow for self-consistent tests of different Dirac plasmon theories.

Here, we image the full phase and amplitude response of graphene plasmons by near-field interferometry of SPPs reflected and scattered by external (edges) and internal boundaries (folds and grain boundaries), as well as defects, of single-layer and multilayer graphene. That complete SPP response in phase and amplitude allows us to develop a simple cavity model that provides a complete, self-consistent, and intuitive description of the optical physics of the graphene plasmons and complements the more complex numerical electrodynamic theories. We derive the plasmon wave vector, damping, and carrier mobility, with values in agreement with theory. We identify spatial inhomogeneities in the local electronic structure associated with the grain boundaries of the exfoliated graphene.

In the spectral region $\hbar\omega < 2E_F$, where Pauli blocking occurs, graphene exhibits a Drude-type behavior [19] and the SPP wave vector is given by [2]:

$$k_{\mathrm{SPP}} = \frac{2\pi h^2 c^2 \epsilon_0 \kappa}{e^2 E_F \lambda_0^2}, \tag{1}$$

where κ is the average dielectric function of the embedding media $\kappa = \kappa_1 + i\kappa_2 = (\epsilon_1 + \epsilon_2)/2$. Figure 1(a) shows the calculated dispersion relation of the graphene SPP using experimental values for the $\mathrm{SiO_2}$ dielectric function [20] and assuming $E_F = 0.4$ eV as an example. The large in-plane momentum necessary to overcome that wave vector mismatch is provided by the evanescent near field of the tip with apex radius $r \propto 1/k_{\mathrm{tip}}$ [9–11]. SPPs are thus launched

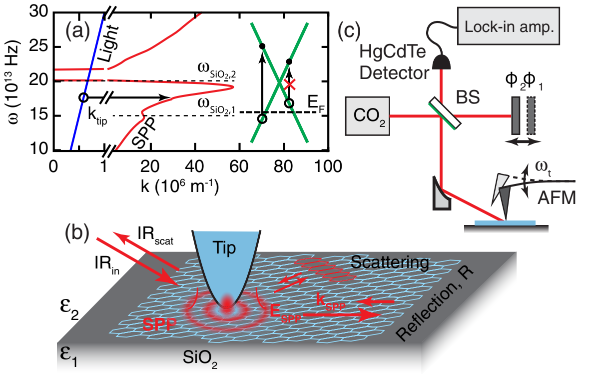

FIG. 1 (color online). (a) Graphene SPP dispersion relation for $E_F = 0.4$ eV. Inset: Pauli blocking arising from a doping-induced Fermi level shift. (b) Illustration of tip-induced SPP excitation and subsequent interference due to the emission of scattered and reflected SPP waves. (c) Schematic of the experimental setup.

and subsequently scattered or reflected at electronic inhomogeneities in the form of, e.g., defects [12], edges [12,13], or other structural discontinuities [14,15], as illustrated in Fig. 1(b). These reflected waves, after propagating back to the tip, interfere with other local near-field signal contributions and are scattered by the tip into the far field, where they are detected [12,13].

We excite the graphene SPP at $\lambda = 10.8\ \mu$m ($\omega_{SPP} = 174$ THz) using a $^{13}CO_2$ laser (Access Laser), off-resonance from the strong damping of the SiO_2 phonons [Fig. 1(a)], and below the graphene optical phonon frequency at $\omega_{ph,gr} = 307$ THz [21–24]. In the experiment, as shown in Fig. 1(c), the laser is focused onto the tip of an atomic force microscope (AFM, Anasys Instruments) operating in tapping mode using an off-axis parabolic mirror ($NA = 0.35$, $P \sim 5$ mW). The tip-scattered near field E_{NF} is homodyne amplified at the HgCdTe detector (Kolmar Technologies) with the reference field E_{ref} of the Michelson interferometer with beamsplitter (BS). The far-field background is suppressed by lock-in demodulation (Zurich Instruments) at the third harmonic of the cantilever frequency [25]. In order to further suppress amplification of the near field by the self-homodyne background E_{bg} with uncontrolled phase [26], a strong reference field $E_{ref}/E_{bg} \geq 10$ is used [27]. By collecting raster-scanned images at two orthogonal reference phases, the full complex valued tip-scattered near field $\tilde{A} = Ae^{i\Phi}$ can be determined with low error [28]. Mechanically exfoliated graphene [29] on SiO_2 was obtained commercially (Graphene Industries).

Figure 2 shows a typical image of a high-aspect ratio graphene wedge, chosen to feature both single-layer and bilayer regions, as indicated in the topography [Fig. 2(a)], with *s*-SNOM amplitude $A = |\tilde{A}|$ [Fig. 2(b)] and phase $\phi = \arg(\tilde{A})$ [Fig. 2(c)]. The detected tip-scattered light is a superposition of the intrinsic sample optical response that is expected to be largely independent of tip position and the SPP waves whose properties are a function of the local environment or geometry. The amplitude thus exhibits a standing wave pattern from the local interference of SPP reflection from both edges of the wedge, with a maximum seen at a distance of $\lambda/4$ in good agreement with previous studies [12,13]. Phase and amplitude standing waves both exhibit a periodicity of $\lambda/2$ and differ by ~90°. A distinct feature is the phase maximum pinned to the edge. The bilayer region (dotted line) at the tapering end of the wedge is characterized by a decreased amplitude, in addition to reduced λ_{SPP}, as seen by a shift of the maxima in both the amplitude and phase (dashed black lines) closer to the edge of the wedge.

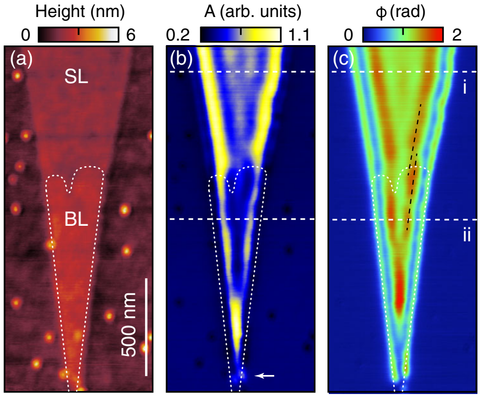

FIG. 2 (color online). (a) AFM topography, (b) near-field amplitude $A = |\tilde{A}|$, and (c) near-field phase $\phi = \arg(\tilde{A})$ of a graphene wedge. The transition from single-layer (SL) to bilayer (BL) graphene is indicated.

Figure 3 shows the corresponding behavior of SPPs at grain boundaries and folds, with the AFM topography [Fig. 3(a)], SPP amplitude [Fig. 3(b)], and phase [Fig. 3(c)] of monolayer graphene with a high density of both kinds of line defects. As seen in both A and ϕ, plasmon reflection and standing wave behavior are observed and are qualitatively similar to that of the external boundaries. The spatial signal variations along the boundaries and within the graphene domains are highly reproducible, including variations in SPP wavelength and amplitude across boundaries.

Previous models described the measured SPP interference images to good agreement [12–15]. However, they relied on complex numerical approaches and did not address the phase. Here, we show that the SPP oscillations can be described in both amplitude and phase simultaneously using a simple phenomenological cavity model

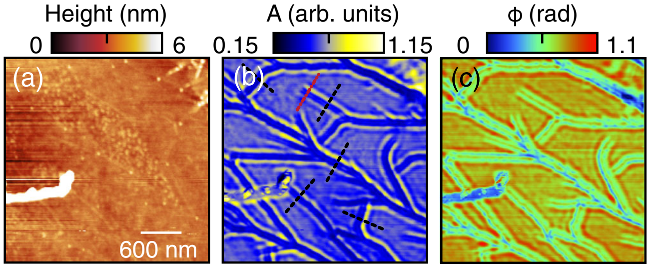

FIG. 3 (color online). (a) AFM topography, (b) near-field amplitude, (c) and near-field phase of a region of single-layer graphene with a high concentration of grain boundaries and folds.

with no independent parameters, as shown schematically in Fig. 4(a). The tip-scattered near-field response of graphene is the sum of a nonresonant dielectric contrast contribution $\tilde{\psi}_{\mathrm{gr}}$, a resonant local tip-induced SPP term $\tilde{\psi}_{\mathrm{SPP},0}$, and the reflected SPP fields $\tilde{\psi}_{\mathrm{SPP},i}$, as

$$\Psi_{\mathrm{gr}} = \tilde{\psi}_{\mathrm{gr}} + \tilde{\psi}_{\mathrm{SPP},0} + \sum_i \tilde{\psi}_{\mathrm{SPP},i}, \tag{2}$$

each with respective amplitude and relative phase. In addition, we consider a SiO_2 substrate near-field response $\tilde{\psi}_{\mathrm{sub}}$. We describe $\tilde{\psi}_{\mathrm{SPP},i} = \tilde{R}_i \times \tilde{\psi}_{\mathrm{SPP},0} \exp\{-2\mathrm{Re}(k_{\mathrm{SPP}}) r_i(\gamma + i)\}$ with decay constant γ, distance between tip and reflection r_i, and complex valued scattering coefficient $\tilde{R}_i$.

In order to account for the finite size of the tip apex generating a spatially averaged near-field response, we use a weighting function Θ convolved with the spatially varying optical response Ψ to simulate the s-SNOM amplitude $\tilde{A}(r) = (\Psi * \Theta)(r)$. As discussed below, we find that treating Θ as Gaussian to approximate the evanescent nature of the tip near field, peaked at r, with a width of 11 nm to model the tip radius, provides good agreement with the experimental results.

Figure 4 shows the simulated spatial distribution of SPP amplitude [Fig. 4(b)] and phase [Fig. 4(c)] for a stationary point source (tip) located at a fixed distance from a reflecting straight boundary located on the left edge (green line). For all calculations, we use $\tilde{\psi}_{\mathrm{gr}} = 0$, $\tilde{\psi}_{\mathrm{SPP},0} = 1$, $\tilde{R} = -1$, and $\gamma = 0.1$. The line cut [Fig. 4(d)] taken along the dashed line separating Figs. 4(b) and 4(c) shows the propagation of the SPP away from the tip and its subsequent perturbation by the reflected SPP. Scanning the tip then results in a parallel standing wave pattern in spatial s-SNOM amplitude [Fig. 4(e)] and phase [Fig. 4(f)], as also seen experimentally. From the line cut [Fig. 4(g)], we see a standing wave period of $\lambda/2$ for both phase and amplitude in agreement with experiment (for details, see the Supplemental Material [30]).

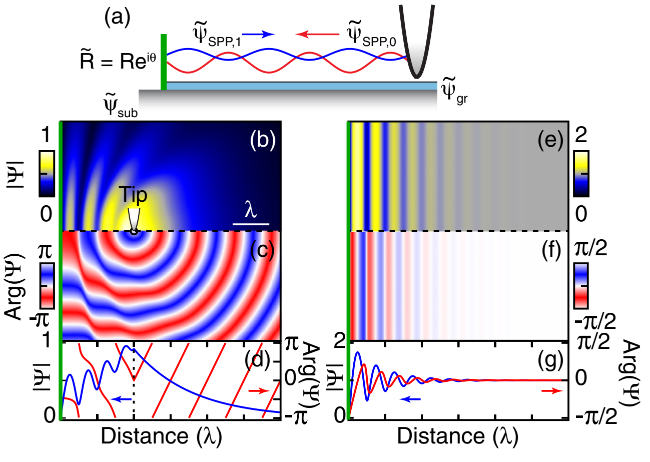

FIG. 4 (color online). (a) Illustration of the graphene SPP cavity model. Calculated SPP distribution of (b) amplitude, (c) phase, and (d) the corresponding line cut along the dashed line, with local tip excitation and reflection from a boundary at the left edge. The resulting spatial standing wave SPP map of s-SNOM (e) amplitude, (f) phase, and (g) line cut when scanning the tip.

We first compare the measured s-SNOM signal with our model by examining line cuts in Fig. 2. Figure 5 shows the experimental phase (solid red line) and amplitude (solid blue line) along dashed lines (i) and (ii) in Fig. 2, with Figs. 5(a) and 5(b) corresponding to single-layer and bilayer graphene, respectively. Graphene edges on both sides are assumed to have identical reflection and decay parameters for $\tilde{\psi}_{\mathrm{SPP},i}$. The dashed grey lines show the results of the model calculations, simultaneously reproducing for just a single parameter set for the single layer and the bilayer, respectively, all the main spatial features both in amplitude and phase. The only exception is a larger than predicted decrease in amplitude at the graphene edge, as discussed below.

The best agreement between theory and experiment is obtained for a reflection coefficient of $\tilde{R} \approx -1$, corresponding to a π phase shift, with a SPP wavelength of $\lambda_{\mathrm{SPP}} = (260 \pm 10)$ nm and $\gamma = 0.25 \pm 0.04$ for the single layer [Fig. 5(a)]. For the bilayer [Fig. 5(b)], we find a shorter wavelength of $\lambda_{\mathrm{SPP}} = (190 \pm 10)$ nm, as discussed below, yet the same damping and reflection coefficients. We further find a phase difference of ~65° between $\tilde{\psi}_{\mathrm{gr}} + \tilde{\psi}_{\mathrm{SPP},0}$ and SiO_2 substrate response $\tilde{\psi}_{\mathrm{sub}}$ for both single-layer and bilayer graphene. This phase shift is less than the 90° expected between the resonant SPP and nonresonant substrate response. However, because graphene does not entirely screen the tip-substrate interaction, signal contributions from the underlying SiO_2 reduce the overall phase shift. While the phases for bilayer and single-layer graphene are identical, an overall smaller amplitude of $\tilde{\psi}_{\mathrm{gr}} + \tilde{\psi}_{\mathrm{SPP},0}$ is found for bilayer graphene.

To model the observed spatial SPP behavior at the different internal interfaces, we examine the line cut in Fig. 3(b) (dashed red line) as an example. The resulting phase and amplitude traces are shown in Fig. 6(a) together with the result of the model (dashed grey lines). Note that the left (right) sides of the boundary have different SPP wavelengths of $\lambda_{\mathrm{SPP}} = 240$ nm (260 nm), as well as different reflection coefficients of $\tilde{R} = 0.45$ (0.55). The different wavelengths and thus wave vectors indicate a possible difference in electronic structure on either side of the linear defects in that region. Variations in reflection coefficients can be explained by the change in SPP wave vector across the boundary, where momentum conservation facilitates

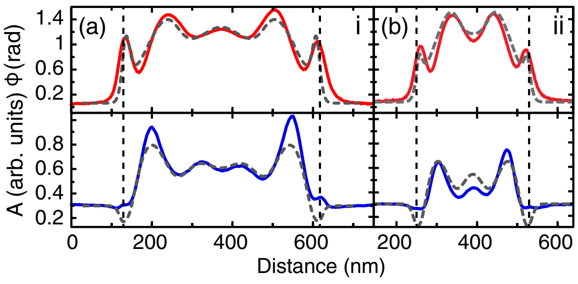

FIG. 5 (color online). Line cuts of phase (solid red line) and amplitude (solid blue line) taken along the dashed lines in Fig. 2 with (i) shown in (a) and (ii) in (b). Dashed lines are fits to the cavity model for a single parameter set.

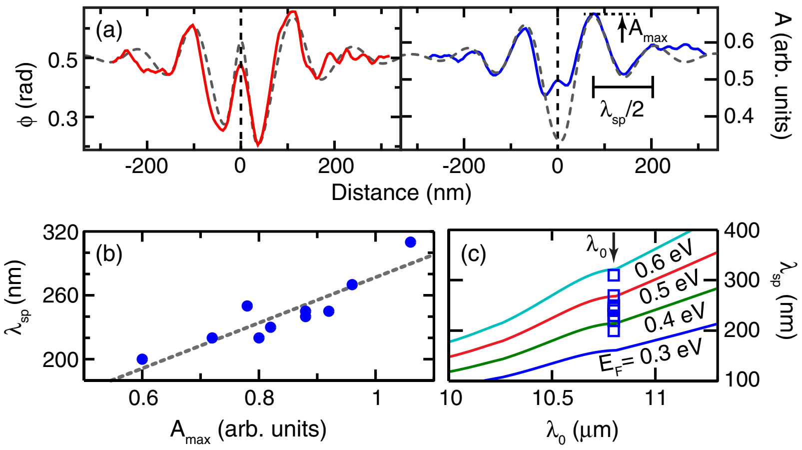

FIG. 6 (color online). (a) Line cut along the dashed red line in Fig. 3 showing phase (solid red line) and amplitude (solid blue line) along with modeled response (dashed grey lines). (b) Plot of SPP wavelength vs amplitude extracted from both sides of the linear defects from Fig. 3. The dashed line is a linear fit. (c) SPP dispersion relation for varying graphene Fermi levels as indicated. The square symbols indicate the range of experimental λ_{SPP} from (b) reflecting the local variations in dopant concentration.

transmission from the high-momentum to low-momentum side similar to material interfaces in conventional optics.

To determine and model possible local variations in electronic properties that underly the complex optical response, Fig. 6(b) shows the relationship between λ_{SPP} and maximum amplitude $A_{\max}$ extracted from both sides of a series of representative boundaries indicated by the dashed black lines in Fig. 3(b). A clear correlation of an increase in SPP intensity $A_{\max}$ with an increase in λ_{SPP} is observed. Since $A_{\max}$ is directly related to the reflection coefficient, this correlation is due to the reduced reflection of high-momentum SPPs.

Using Eq. (1), we can relate that variation in SPP wavelength to local variations in the Fermi level. Shown in Fig. 6(c) are the calculated SPP dispersion relations of graphene on $\mathrm{SiO_2}$ for different values of E_F. The blue squares indicate the range of wavelengths from Fig. 6(b), thus corresponding to spatial variations in E_F of up to 0.2 eV. The Fermi level directly relates to the doping concentration n as $E_F = \hbar v_F k_F$, with Fermi velocity $v_F \approx 1 \times 10^6$ m/s and Fermi momentum $k_F = \sqrt{\pi n}$ [31]. Our spatial variations in Fermi level of $E_F \approx 0.4$–0.6 eV thus correspond to n, ranging from 1.2 to $2.6 \times 10^{13}\ \mathrm{cm^{-2}}$.

The large variation in doping across the boundaries indicates that the reduced conductivity of boundaries [14,32] prevents charge equilibration between adjacent sides. Unlike the charge carriers themselves, the SPPs as collective excitations are able to traverse such potential barriers as seen by the nonunity reflection coefficients.

We then determine the carrier mobility from the experimentally obtained damping γ. By correcting for the superposition of Ohmic damping and radial decay from the excitation point, we obtain an Ohmic SPP decay constant of $\gamma_p = 0.12 \pm 0.04$. Using $\gamma_p \approx \sigma_1/\sigma_2 + \kappa_2/\kappa_1$, with graphene conductivity $\sigma = \sigma_1 + i\sigma_2$ [12] and $\kappa_2/\kappa_1 = 0.04$, this results in a carrier relaxation rate $\Gamma = \sigma_1\omega/\sigma_2 = (14 \pm 4)$ THz. The relaxation rate then relates to the mobility $\mu = e v_F / \Gamma \hbar k_F$ [2], giving $\mu = 1.6 \times 10^3\ \mathrm{cm^2\,V^{-1}\,s^{-1}}$.

Our derived mobility is in good agreement with previous s-SNOM measurements [12,13] but lower than typical values for exfoliated samples, as determined by transport measurements [33]. Similarly, our values for E_F and n agree with values derived by s-SNOM [12,13], but they and the variations seen due to charge pooling are larger than expected [31,33–35]. Recent work has attributed the discrepancy in damping rates and thus mobility to the large SPP frequency and associated wave vectors, which result in increased in impurity scattering and therefore deviations from assumed dc values [36]. The surprisingly large Fermi energy has not been addressed in this work.

Our results provide insight into the spatial phase behavior of graphene SPPs. The phase is robust to changes in signal intensity due to the presence of, e.g., bilayer graphene, as seen in Fig. 2, or the presence of surface contaminants that otherwise reduce the amplitude signal (see Supplemental Material [30]). The optical phase also provides an additional constraint for our cavity model. In particular, the absence of independent parameters used to describe the amplitude and phase underscores its validity. Despite its simplicity, good semiquantitative agreement is found between the model and the data including the phase relationship between the amplitude and phase. However, the overall agreement in the amplitude near the edges is seen to decrease with dips in the model and spatial shifts in the oscillation extrema. This can be attributed to changes in local electronic structure [12] and field variations near the edges [13] and emphasizes the high sensitivity of SPP near-field interferometry to such small inhomogeneities.

We note that our parameters do not reproduce the dual peaks resulting from the localized mode indicated near the wedge terminus by a white arrow in Fig. 2(b). It is expected that gradually tapered wedges as studied here exhibit phenomena similar to nanoribbons, where a width-dependent reflection phase has been predicted [37]. However, we find a constant reflection coefficient [24], as evidenced by the interference maximum in the phase at the graphene edge which we see to abruptly transform into a localized mode which can only be reproduced through the use of $\tilde{R} = 1$, as noted previously [13].

In addition to the long range Dirac plasmons readily observed in the Pauli-blocking regime, additional acoustic and nonlinear modes exist [38–40]. While these may be difficult to observe with optical means due to the strong damping and large momenta required, these may be observable using near-field excitations at higher photon energies and can readily be studied using electron-based techniques [41,42].

In conclusion, the full amplitude and phase spatially resolved imaging of graphene SPPs that are scattered and reflected by discontinuities such as edges, grain boundaries, and defects provides nanoscale insight into local electronic structure and dynamics in graphene. As the amplitude and phase couple differently to the reflection coefficients and doping, their simultaneous measurement allows us to develop a self-consistent phenomenological cavity model with no adjustable parameter to describe the SPP response. We observe the effects of charge pooling and associated Fermi level offsets in sample regions with a high density of grain boundaries and folds. These results highlight the need for nanoscale control of electronic structure for optimal graphene optical and electronic device performance.

The authors thank Greg Andreev for stimulating this study, as well as Joanna Atkin for fruitful discussions. This research was supported by the U.S. Department of Energy, Office of Basic Energy Sciences, Division of Materials Sciences and Engineering, under Award No. DE-FG02-12ER46893. J. A. G. and S. B. contributed equally to this work.

---

[*]Present address: National Institute of Standards and Technology, Boulder, CO 80305, USA.
[†]markus.raschke@colorado.edu

[1] E. H. Hwang and S. Das Sarma, Phys. Rev. B **75**, 205418 (2007).
[2] M. Jablan, H. Buljan, and M. Soljacic, Phys. Rev. B **80**, 245435 (2009).
[3] L. Ju, B. Geng, J. Horng, C. Girit, M. Martin, Z. Hao, H. A. Bechtel, X. Liang, A. Zettl, Y. R. Shen, and F. Wang, Nat. Nanotechnol. **6**, 630 (2011).
[4] H. Yan, X. Li, B. Chandra, G. Tulevski, Y. Wu, M. Freitag, W. Zhu, P. Avouris, and F. Xia, Nat. Nanotechnol. **7**, 330 (2012).
[5] R. Roldán and L. Brey, Phys. Rev. B **88**, 115420 (2013).
[6] A. N. Grigorenko, M. Polini, and K. S. Novoselov, Nat. Photonics **6**, 749 (2012).
[7] K. A. Velizhanin and A. Efimov, Phys. Rev. B **84**, 085401 (2011).
[8] F. H. L. Koppens, D. E. Chang, and F. J. García de Abajo, Nano Lett. **11**, 3370 (2011).
[9] B. Hecht, H. Bielefeldt, L. Novotny, Y. Inouye, and D. W. Pohl, Phys. Rev. Lett. **77**, 1889 (1996).
[10] X. Ren, A. Liu, C. Zou, L. Wang, Y. Cai, F. Sun, G. Guo, and G. Guo, Appl. Phys. Lett. **98**, 201113 (2011).
[11] Z. Fei, G. O. Andreev, W. Bao, L. M. Zhang, A. S. McLeod, C. Wang, M. K. Stewart, Z. Zhao, G. Dominguez, M. Thiemens *et al.*, Nano Lett. **11**, 4701 (2011).
[12] Z. Fei, A. S. Rodin, G. O. Andreev, W. Bao, A. S. McLeod, M. Wagner, L. M. Zhang, Z. Zhao, M. Thiemens, G. Dominguez *et al.*, Nature (London) **487**, 82 (2012).
[13] J. Chen, M. Badioli, P. Alonso-González, S. Thongrattanasiri, F. Huth, J. Osmond, M. Spasenovic, A. Centeno, A. Pesquera, P. Godignon *et al.*, Nature (London) **487**, 77 (2012).
[14] Z. Fei, A. S. Rodin, W. Gannett, S. Dai, W. Regan, M. Wagner, M. K. Liu, A. S. McLeod, G. Dominguez, M. Thiemens *et al.*, Nat. Nanotechnol. **8**, 821 (2013).
[15] J. Chen, M. L. Nesterov, A. Y. Nikitin, S. Thongrattanasiri, P. Alonso-González, T. M. Slipchenko, F. Speck, M. Ostler, T. Seyller, I. Crassee *et al.*, Nano Lett. **13**, 6210 (2013).
[16] Z. H. Ni, T. Yu, Y. H. Lu, Y. Y. Wang, Y. P. Feng, and Z. X. Shen, ACS Nano **2**, 2301 (2008).
[17] R. Sensarma, E. H. Hwang, and S. Das Sarma, Phys. Rev. B **82**, 195428 (2010).
[18] K. F. Mak, J. Shan, and T. F. Heinz, Phys. Rev. Lett. **104**, 176404 (2010).
[19] Z. Q. Li, E. A. Henriksen, Z. Jiang, Z. Hao, M. C. Martin, P. Kim, H. L. Stormer, and D. N. Basov, Nat. Phys. **4**, 532 (2008).
[20] *Handbook of Optical Constants of Solids*, edited by E. Palik (Springer, Berlin, 2000).
[21] M. Jablan, M. Soljacic, and H. Buljan, Phys. Rev. B **83**, 161409(R) (2011).
[22] A. Politano, V. Formoso, and G. Chiarello, J. Phys. Condens. Matter **25**, 345303 (2013).
[23] H. Yan, T. Low, W. Zhu, Y. Wu, M. Freitag, X. Li, F. Guinea, P. Avouris, and F. Xia, Nat. Photonics **7**, 394 (2013).
[24] V. W. Brar, M. S. Jang, M. Scherrott, J. J. Lopez, and H. A. Atwater, Nano Lett. **13**, 2541 (2013).
[25] F. Keilmann and R. Hillenbrand, Phil. Trans. R. Soc. A **362**, 787 (2004).
[26] S. Aubert, A. Bruyant, S. Blaize, R. Bachelot, G. Lerondel, S. Hudlet, and P. Royer, J. Opt. Soc. Am. B **20**, 2117 (2003).
[27] A. C. Jones, R. L. Olmon, S. E. Skrabalak, B. J. Wiley, Y. N. Xia, and M. B. Raschke, Nano Lett. **9**, 2553 (2009).
[28] S. Berweger, D. M. Nguyen, E. A. Muller, H. A. Bechtel, T. T. Perkins, and M. B. Raschke, J. Am. Chem. Soc. **135**, 18292 (2013).
[29] K. S. Novoselov, D. Jiang, F. Schedin, T. J. Booth, V. V. Khotevich, S. V. Morozov, and A. K. Geim, Proc. Natl. Acad. Sci. U.S.A. **102**, 10451 (2005).
[30] See Supplemental Material at http://link.aps.org/supplemental/10.1103/PhysRevLett.113.055502 for further discussion of the model and observed phenomena, and data of SPP scattering from a point-like defect.
[31] A. H. Castro Neto, F. Guinea, N. M. R. Peres, K. S. Novoselov, and A. K. Geim, Rev. Mod. Phys. **81**, 109 (2009).
[32] L. Tapaszto, P. Nemes-Incze, G. Dobrik, K. J. Yoo, C. Hwang, and L. O. Biro, Appl. Phys. Lett. **100**, 053114 (2012).
[33] A. K. Geim and K. S. Novoselov, Nat. Mater. **6**, 183 (2007).
[34] J. Martin, N. Akerman, G. Ulbricht, T. Lohmann, J. H. Smet, K. von Klitzing, and A. Yacoby, Nat. Phys. **4**, 144 (2008).
[35] Y. Zhang, V. W. Brar, C. Girit, A. Zettl, and M. F. Crommie, Nat. Phys. **5**, 722 (2009).
[36] A. Principi, G. Vignale, M. Carrega, and M. Polini, Phys. Rev. B **88**, 121405(R) (2013).
[37] J. Christensen, A. Manjavacas, S. Thongrattanasiri, F. H. L. Koppens, and F. J. García de Abajo, ACS Nano **6**, 431 (2012).
[38] Y. Gao and Z. Yuan, Solid State Commun. **151**, 1009 (2011).
[39] M. Pisarra, A. Sindona, P. Riccardi, V. M. Silkin, and J. M. Pitarke, arXiv:1306.6273v3.
[40] A. Politano and G. Chiarello, Carbon **71**, 176 (2014).
[41] T. Langer, D. F. Förster, C. Busse, T. Michely, H. Pfnür, and C. Tegenkamp, New J. Phys. **13**, 053006 (2011).
[42] C. Tegenkamp, H. Pfnür, T. Langer, J. Baringhaus, and H. W. Schumacher, J. Phys. Condens. Matter **23**, 012001 (2011).